Ceramics International 49 (2023) 7524–7533

Contents lists available at ScienceDirect

Ceramics International

journal homepage: www.elsevier.com/locate/ceramint

Highly-doped YAG:Sm^{3+} transparent ceramics: Effect of Sm^{3+} ions concentration

A.D. Timoshenko [a,*], O.O. Matvienko [a], A.G. Doroshenko [a], S.V. Parkhomenko [a], I.O. Vorona [a], O.S. Kryzhanovska [a], N.A. Safronova [a], O.O. Vovk [a], A.V. Tolmachev [a], V.N. Baumer [b], I. Matolínová [c], S. Hau [d], C. Gheorghe [d], R.P. Yavetskiy [a]

[a] Institute of Single Crystals, NAS of Ukraine, 60 Nauky Ave., Kharkiv, 61072, Ukraine
[b] SSI "Institute for Single Crystals", NAS of Ukraine, 60 Nauky Ave., Kharkiv, 61072, Ukraine
[c] Charles University, Faculty of Mathematics and Physics, V Holešovičkách 2, Prague, 18000, Czech Republic
[d] National Institute for Laser, Plasma and Radiation Physics, Laboratory of Solid-State Quantum Electronics, Magurele, 077125, Ilfov, Romania

ARTICLE INFO

Keywords:
Ceramics
Microstructure
Optical properties
Optical spectroscopy
Sintering
X-ray diffraction

ABSTRACT

YAG:Sm^{3+} (3–15 at.%) transparent ceramics, a promising cladding material for suppressors of parasitic oscillations at 1064 nm of YAG:Nd^{3+} lasers, have been prepared by solid-state reactive sintering at 1725 °C. The effect of samarium ions concentration on the microstructure and optical properties of YAG:Sm^{3+} sintered ceramics was studied for the first time. The solubility limit of samarium ions in the garnet matrix was found to lie within the range of 9–11 at.%. The spectroscopic characterization of YAG:Sm^{3+} (3–15 at.%) ceramic samples showed that the absorption coefficients corresponding to Sm^{3+} ions transitions increased linearly with increasing Sm^{3+} doping. Also, the increase in the concentration of Sm^{3+} ions contributes to the increase in the intensities of the satellites, leading to the broadening of the main spectral lines and implicitly to the increase of the absorption coefficient around 1064 nm. It was shown that YAG:Sm^{3+} ceramics doped with 9 at.% Sm^{3+} ions possess optical losses of 0.07 cm^{-1} at 808 nm and an optical absorption coefficient of 4.45 cm^{-1} at 1064 nm. The concentration dependence of the $^4G_{5/2}$ level decay confirmed that the luminescence extinction is due to the energy transfer between the Sm^{3+} ions through cross-relaxation processes. All these results show that highly-doped YAG:Sm^{3+} (9 at.%) ceramics could be the best candidate for parasitic oscillation suppression in high-power YAG:Nd^{3+} lasers at 1064 nm.

1. Introduction

Nowadays, the optimization of the architecture of active media and the miniaturization of high-power IR laser systems constitute an active research and development area of laser material science. Since the first observations of the trivalent rare-earth ions doped yttrium aluminum garnet (YAG:RE^{3+}) ceramics [1], considerable progress has been achieved in the improvement of their optical transparency [2,3] and thermal and mechanical properties [4–7]. The advantages of YAG:RE^{3+} polycrystalline ceramics as an active laser medium include not only lower fabrication cost and improved processability, but also the possibility to create promising compact solid-state lasers with high efficiency due to the higher doping levels available. This is important because the short length of the resonator in a microchip laser (L~0.1–10 mm) requires a high concentration of active ions in the active medium and Q-switching modulator, which is difficult or even impossible to achieve with existing single-crystal growing technologies [8–12]. Recently, YAG:Yb^{3+} [13–18] and YAG:Nd^{3+} [19–23] transparent ceramics having excellent laser properties have been reported. The peculiarities of sintering mechanisms and the diffusion mobility of grain boundaries at high temperatures have been established [24–26]. Despite the considerable progress achieved, several key challenges in the practical implementation of such ceramic materials were revealed. Parasitic oscillations and amplified spontaneous emission are among the main factors decreasing the optical efficiency of diode-pumped solid-state lasers. The formation of composite ceramics (i.e. cladding) is considered one of the most promising techniques to reduce the influence of these factors, even though decreasing RE^{3+} doping concentration could hinder these effects to some extent [27–30]. Mechanical strength, effective suppression of parasitic oscillations, as well as the possibility of

* Corresponding author.
E-mail address: tymoshenko@isc.kharkov.ua (A.D. Timoshenko).

https://doi.org/10.1016/j.ceramint.2022.10.257
Received 16 July 2022; Received in revised form 11 October 2022; Accepted 19 October 2022
Available online 23 October 2022
0272-8842/© 2022 The Authors. Published by Elsevier Ltd. This is an open access article under the CC BY-NC-ND license (http://creativecommons.org/licenses/by-nc-nd/4.0/).

defect-free bonding are the main criteria put forward for the cladding material. Taking into account their optical properties, YAG:Sm^{3+} transparent ceramics are considered the best candidate for the suppression of parasitic oscillation in high-power YAG:Nd^{3+} lasers [31–34]. Recently, Zhu and co-workers [29] designed and built an actively Q-switched laser with zig-zag slab architecture based on YAG:Nd^{3+}/YAG:Sm^{3+} diffusively-bonded crystals. The fabricated active Q-switched laser demonstrated pulse energy of 104 mJ and optical conversion efficiency of 30.5%. Thus, YAG:Sm^{3+} is a promising material for the suppression of parasitic oscillations and amplified spontaneous emission of YAG:Nd^{3+} lasers.

The influence of Sm^{3+} ions concentration on the sintering evolution and the optical properties of YAG:Sm^{3+} ceramics has not been thoroughly investigated up to now. Ali et al. [35] studied the effect of Sm^{3+} ions concentration on the spectroscopic and optical properties of co-precipitated YAG:Sm^{3+} nanocrystalline powders. The formation of the secondary phases in YAG:Sm^{3+} nanopowders was not detected by XRD in the Sm^{3+} ions concentration range from 0.5 to 8 mol.%. In [36], it was reported that the structural homogeneity of YAG:Sm^{3+} obtained by the sol-gel method is preserved up to Sm^{3+} concentrations of ≈30 at.% of Sm^{3+} ions. Further increase of doping concentration leads to the formation of inclusions of the perovskite phase $SmAlO_3$ (SmAP). Thus, $Sm_3Al_5O_{12}$ is not stable and the solubility of Sm^{3+} ions in the dodecahedral YAG position is predicted to be less than 100%. Němec et al. [37] reported optical properties of YAG:Sm^{3+} single crystals doped with various Sm^{3+} ions concentrations from 1 at.% up to 20 at.%. However, until now, the phase composition of the crystals and the solubility limit of samarium ions were not reported.

Recently, we have studied the effect of the sintering temperature on the microstructure and optical properties of reactively-sintered YAG:Sm^{3+} (5 at.%) ceramics [38]. In the present study, the effects of Sm^{3+} ions concentrations on the structural-phase state and optical properties of reactive sintered YAG:Sm^{3+} ceramics at the optimal sintering temperature were investigated in detail. The solubility limit of Sm^{3+} ions in YAG was also estimated. It should be noted that the sintering peculiarities of highly-doped YAG:Sm^{3+} ceramics may change significantly in comparison with the well-known YAG:Nd^{3+} and YAG:Yb^{3+} ceramics due to differences in ionic radii, electronegativity, atomic number, and tendency to change the valence state of dopants under vacuum sintering.

2. Experimental procedures

2.1. Preparation of YAG:Sm^{3+} ceramics

High-purity commercial powders were used as starting materials for obtaining YAG:Sm^{3+} ceramics: α-Al_2O_3 (>99.99%, d = 0.15–0.25 μm, Baikowski, France), Y_2O_3 (99.999%, d ~ 5 μm, Alfa Aesar, USA) and Sm_2O_3 (>99.99%, d ~ 5 μm, Alfa Aesar, USA). As a sintering additive, 0.5 wt% TEOS (≥99.999%, Alfa Aesar) was used. The mixed powders of stoichiometric composition YAG:Sm^{3+} containing from 3 up to 15 at.% of samarium ions were ball-milled with a planetary mill Fritsch Pulverisette 5/4 for 15 h using 10 mm corundum balls, 250 ml corundum jar, and absolute ethanol as solvent. The rotation speed was 140 rpm, and the ball-to-powder volume ratio was 7. The obtained suspensions were dried at 60°C for 10 h and sieved through a 200-mesh sieve before the powder mixtures were annealed at 600°C for 4 h in air to remove residual organics. The green bodies were formed by uniaxial pressing at 50 MPa followed by cold isostatic pressing at 250 MPa and then annealing in air at 800 °C for 4 h. YAG:Sm^{3+} ceramics were produced by the reactive vacuum sintering at 1725°C for 10 h at 10^{-3} Pa. The sintered ceramics were cooled to room temperature with a cooling rate of 500 °C/h. After sintering, the ceramics were annealed in air at 1300 °C for 15 h to recover oxygen stoichiometry and to remove residual mechanical stresses. The obtained ceramics were polished on both surfaces using lint-free cloths with diamond micro powders slurries. The samples for microstructural studies were thermally etched at 1400 °C for 15 h after polishing.

2.2. Microstructural and optical characterization of YAG:Sm^{3+} ceramics

The phase composition of YAG:Sm^{3+} ceramics was studied by X-ray diffraction (XRD) using a D-500 diffractometer with CuK_α-radiation (Siemens AG, Germany). The Rietveld refinement was performed with the FullProf program. The lattice parameter was calculated with FullProf using a powder pattern of LaB_6 to obtain the instrumental profile function. The microstructure of the sintered YAG:Sm^{3+} ceramics was studied by optical microscopy in reflected light mode (Primotech, Carl Zeiss, Germany). The average grain size of ceramics was determined by using the linear intercept method by analyzing at least 500 grains for each measurement.

The morphology and elemental composition of the ceramic samples were studied by means of field-emission scanning electron microscopy (FESEM) and energy-dispersive X-ray spectroscopy (EDX). The microscope (Tescan Mira3) was equipped with a Bruker XFlash detector operating at a primary electron energy of 30 keV (16 mm working distance and 4 nm spot size). To avoid the effect of charging the ceramic samples during the measurement, their surface was covered by a 6–8 nm thick carbon layer by magnetron sputtering. 100 μm^2 area or point EDX analysis was performed to monitor changes in the composition of volume and secondary phases, respectively. The elemental concentrations in a given sample are calculated with an error of about 10%.

For the spectroscopic investigations, a halogen lamp, a Xe lamp, and an adjustable laser OPOTEK RADIANT 355 LD Parametric optical oscillator (OPO) in the range of 410–2500 nm operated at 10 Hz were used as excitation sources. The detection systems consist of a Ge detector and an S20 photomultiplier attached to the Horiba Jobin Yvon and Jarrell-Ash Czerny monochromators, respectively. These are connected with a lock-in amplifier and online with a computer. A 2024B Tektronix oscilloscope (sample rate 2 GS/s, vertical resolution 8 bits, analog bandwidth 200 MHz) has been used for emission decay data acquisition. The decay curves were measured at 617 nm under 465 nm excitation from the OPO laser.

The in-line optical transmittance spectra of YAG:Sm^{3+} ceramics were measured with a Lambda-35 spectrophotometer (Perkin-Elmer, USA) over the 0.2–1.1 μm wavelength range. The optical losses, α, were calculated from the measured transmittance, considering surface reflection from both sides and the returned 2-times reflected light:

$$\alpha = \frac{1}{L}\ln\left(\frac{(1-R)^2*(1+R)^2}{T}\right) \quad (1)$$

where T is the measured transmittance, L is the sample length in the direction of light propagation, and R is the Fresnel reflection (normal incidence case).

3. Results and discussion

3.1. Phase composition and microstructure of YAG:Sm^{3+} (3–15 at.%) ceramics

Fig. 1 shows the photographs of YAG:Sm^{3+} polished transparent ceramic samples containing 3–15 at.% samarium ions obtained by vacuum sintering at 1725 °C. It can be seen that the samples have a light-yellow color and are characterized by a high degree of optical transparency, as the letters under the samples can be clearly read through the 3 mm thick specimens. The intensity of the yellow color increases with increasing samarium ions concentration, indicating the gradual incorporation of Sm^{3+} ions into the crystalline structure of YAG matrix within the concentration range investigated.

The analysis of the X-Ray diffraction spectra on the obtained YAG:Sm^{3+} transparent ceramics shows that all the specimens in the 3–15 at.% concentration range of samarium ions appear to be single-phase indexed

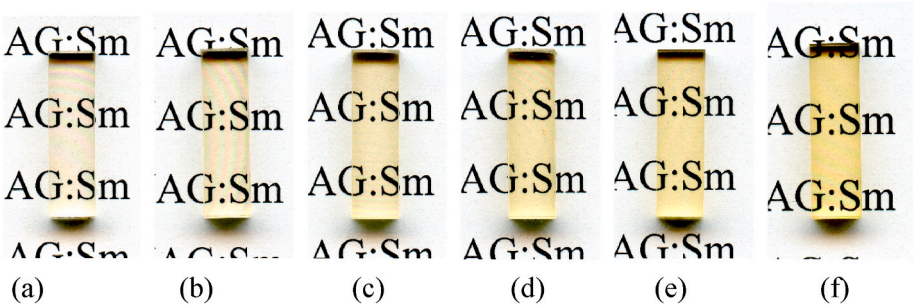

Fig. 1. Photographs of polished YAG:Sm^{3+} ceramics (3 mm in thickness) sintered at 1725°C and doped by 3 at.% (a), 5 at.% (b), 7 at.% (c), 9 at.% (d), 11 at.% (e), and 15 at.% (f) of samarium ions.

by cubic YAG (JPCDS card No. 33-0040). No secondary phases were detected in the concentration range studied. This means that $(Y_{1-x}Sm_x)_3Al_5O_{12}$ ($Y_{1-x}Sm_xAG$) substitutional solid solutions are formed within the error of the XRD method of 1 wt%. Fig. 2a shows a typical diffraction pattern obtained for YAG:Sm^{3+} 15 at.% ceramics. The sample exhibits sharp diffraction peaks, indicating its excellent crystallinity after sintering.

The lattice constant, *a*, of YAG:Sm^{3+} ceramics as a function of Sm^{3+} ions concentration is given in Fig. 2b. The unit cell parameter increases linearly from 12.01055 Å up to 12.02937 Å with increasing activator concentration from 3 at.% up to 15 at.%, according to Vegard's rule. This behavior is caused by the higher ionic radius of Sm^{3+} ions (1.079 Å) in the dodecahedral position of the garnet structure compared with Y^{3+} ions (1.019 Å). The difference between the ionic radii of Y^{3+} and Sm^{3+} ions does not exceed 10%, so the substitution of Y^{3+} ions with Sm^{3+} ones is accompanied by the formation of solid solutions with higher lattice parameters in comparison with undoped YAG ($a = 12.0091(2)$ Å, JCPDS card No.33-40).

Next, we will attempt to compare the experimental and theoretical values of the lattice parameter for as-sintered $Y_{1-x}Sm_xAG$ substitutional solid solutions. Up to now, the data on the practical synthesis and characteristics of both single-crystalline or ceramic $Sm_3Al_5O_{12}$ are not available because of the thermodynamic instability relative to SmAP and Al_2O_3 [36,39]. The theoretical estimation of the crystal lattice parameter of solid solutions was performed according to [40,41]:

$$a_S = 7.029540 + 3.312770r_A + 2.493980r_B + 3.341240r_C - 0.877580r_Ar_B - 1.387770r_Ar_C \quad (2)$$

where a_s is the theoretical crystal lattice parameter, and r_A, r_B, and r_C are the Shannon ionic radii for the atoms in the A, B, and C positions characteristic to the $A_3B_2C_3O_{12}$ garnet-type structure [42,43]. The lattice parameter for $Sm_3Al_5O_{12}$ calculated using equation (2) was found to be 12.1508 Å. As can be seen from Fig. 2b, the theoretical lattice parameter is slightly higher than the experimental one for lower concentrations of samarium ions, which may be due to the presence of SiO_2 sintering aid. It is well-known that sintering of YAG using SiO_2 additive leads to substitution of Al^{3+} (0.53 Å) ions by smaller Si^{4+} ions (0.4 Å) in the garnet structure, resulting in a decrease of lattice parameter in comparison with Si^{4+}-undoped YAG ceramics [44].

Surface morphologies of reactive-sintered YAG:Sm^{3+} (3–15 at.%) ceramics are shown in Fig. 3 and are characterized by a homogenous microstructure containing only a few pores and surface irregularities (not shown) up to 5 μm, while flat grain boundaries indicate the completion of the sintering process [45]. No abnormal grain growth was detected from any of the obtained specimens. Secondary phases along grain boundaries or in triple junctions were not detected in YAG:Sm^{3+} ceramics doped with 3 up to 9 at.% samarium ions, pointing out the complete insertion of samarium ions into the YAG structure with the formation of a substitutional solid solution. Additional phases were revealed for the samples doped with 11 at.% and 15 at.% Sm^{3+} ions (Figs. 3e and f and 4a-c). The appearance of secondary phases may indicate a decomposition of $Y_{1-x}Sm_xAG$ supersaturated substitutional solid-solution.

The results obtained by energy-dispersive X-ray spectroscopy (EDX) on all studied YAG:Sm^{3+} ceramics are presented in Table 1. The content of the constituent elements (Y, Al, O, Sm) is well described by the YAG stoichiometry within the error of the method. However, the secondary phase revealed in the YAG:Sm^{3+} (≥11 at.%) (Figs. 4a and b) contains an

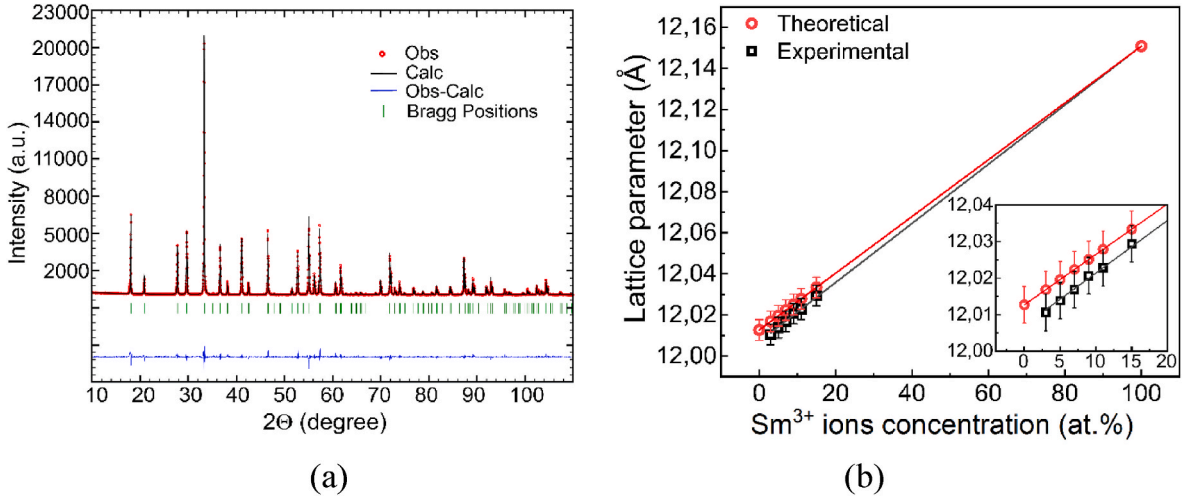

Fig. 2. Typical XRD pattern of YAG:Sm^{3+} (15 at.%) ceramics sintered at 1725 °C for 10 h (a); experimental and theoretical lattice parameter of YAG:Sm^{3+} ceramics as a function of Sm^{3+} ions concentration (b). The inset shows the variation of the lattice parameter in the concentration range of 0–15 at.% of Sm^{3+} ions.

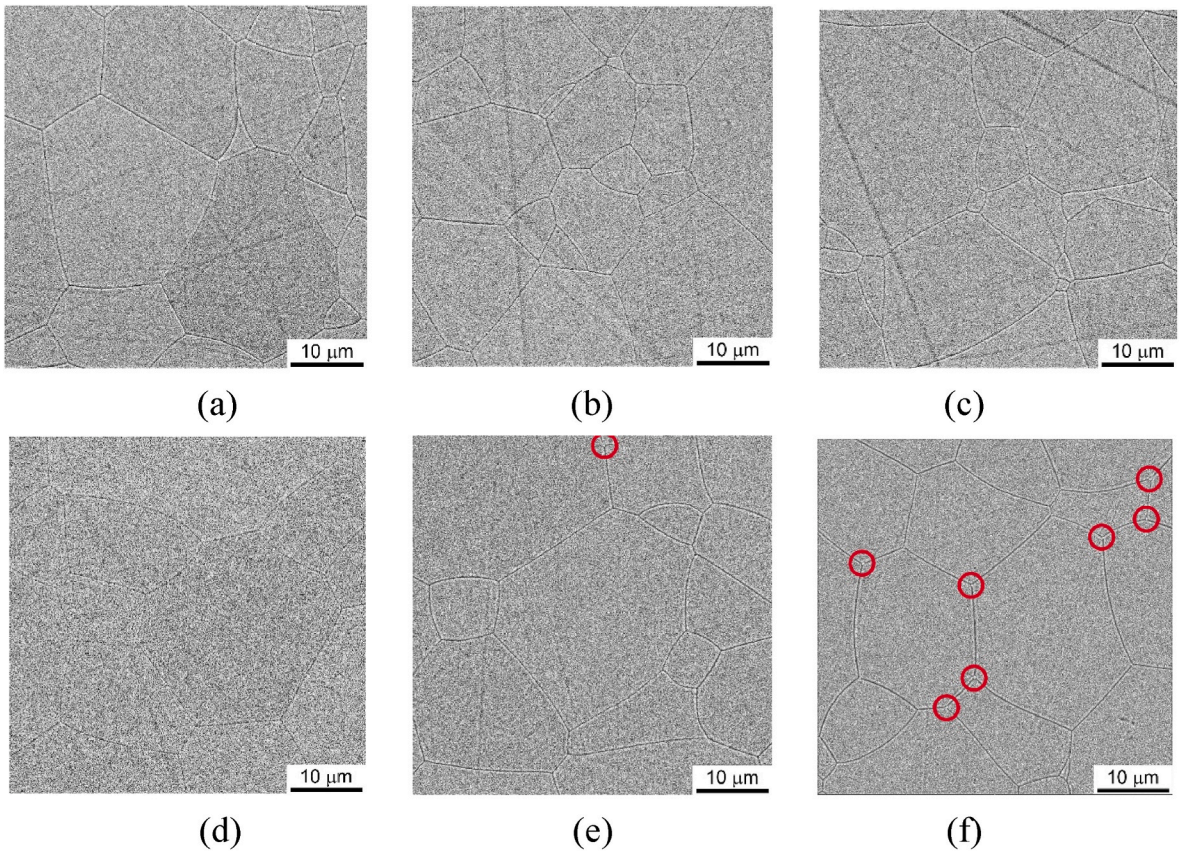

Fig. 3. FESEM surface morphology of YAG:Sm^{3+} transparent ceramics sintered at 1725°C and doped with 3 at.% (a), 5 at.% (b), 7 at.% (c), 9 at.% (d), 11 at.% (e), and 15 at.% (f) of samarium ions. Red circles indicate places of occurrence of the secondary phase. (For interpretation of the references to color in this figure legend, the reader is referred to the Web version of this article.)

increased amount of Sm, in addition to the detected silicon and calcium (Fig. 4d and Table 2). We suppose that the presence of trace amounts of calcium in the secondary phase is associated with the contamination of polished ceramics during thermal etching in 99.7% purity alumina crucibles. Also, the (Y + Sm)/Al ratio is slightly higher than the ratio found for the volume phase (cf. Tables 1 and 2). The (Y + Sm)/Al ratio for the secondary phase based on point EDX analysis was found to be 0.75, which has the stoichiometry shifted to the perovskite $Y_{1-x}Sm_xAlO_3$ phase ((Y + Sm)/Al = 1) as compared with 0.6 for (Sm + Y)AG. However, in the case of relatively small formations, the point EDS analysis may give a distorted idea of its composition, as part of the EDX signal also comes from the volume phase. One can assume that if Sm content in YAG exceeds the solubility limit, the decomposition of $Y_{1-x}Sm_xAG$ solid solution into $Y_{1-x}Sm_xAlO_3$ perovskite and Al_2O_3 takes place, but also more complex mechanisms can appear. Thus, XRD analysis, as well as FESEM and EDS data, allow one to conclude that the solubility limit of Sm^{3+} ions in the crystalline structure of YAG polycrystalline ceramics lies within the concentration range of 9–11 at.%. These values are significantly higher than those for YAG:Sm^{3+} single crystal grown from the melt (5-6 at. %), estimated considering the effective distribution coefficient of Sm^{3+} ions [37,46,47]. It should be noted that the highest samarium ions concentration in YAG was previously reported to be 13–18 at.% for relatively thin epitaxial single-crystal layers obtained by hydrothermal crystal growth technique on undoped YAG substrates [48].

The grain size distribution in the YAG:Sm^{3+} ceramics doped with different concentrations of Sm^{3+} ions, as well as the average grain size calculated from FESEM analysis are presented in Fig. 5. The average grain size of YAG:Sm^{3+} transparent ceramics has an inverse dependence on Sm^{3+} ions content and decreases from 24 to 18 μm while the activator concentration rises from 3 to 15 at.%. A similar dependence was observed for YAG:Nd^{3+} laser ceramics [49,50]. This effect can be attributed to the deformation of the crystal lattice due to the larger ionic radius of Sm^{3+} (0.122 Å) compared to Y^{3+} (0.116 Å) and the corresponding reduction of the volume diffusion coefficient of rare earth ions. Given the higher solubility of dopants at the grain boundaries compared to the ceramics' volume, segregation of cations at the grain boundaries can occur [51], which in turn reduces the surface energy and mobility of the grain boundaries. The dopant segregation at the grain boundaries is higher as the effective distribution coefficient in the solid and liquid phases is lower [52]. The effective distribution coefficient of Sm^{3+} ions in YAG is 0.3–0.4 [47,53,54], and therefore it is likely that partial segregation of Sm^{3+} ions at grain boundaries occurs. Thus, increasing the samarium doping inhibits the coarsening of YAG:Sm^{3+} ceramics.

3.2. Optical properties of YAG:Sm^{3+} (3–15 at.%) ceramics

The absorption spectra of Sm^{3+} ions in the visible domain of YAG:Sm^{3+} transparent ceramics doped with different concentrations of samarium ions (3, 5, 7, 9, 11, and 15 at.%) were measured at room temperature and are shown in Fig. 6. The most intense line at ~405.5 nm corresponds to the $^6H_{5/2}\rightarrow{}^6P_{3/2,}\ ^6P_{5/2}$ transitions of Sm^{3+} ions, and the rest of the transitions are similar to those identified in the case of Sm^{3+}-doped YAG nanocrystals with much lower doping concentrations [54]. The particular interest in this range is due to the spectral matching with commercial InGaN/GaN laser diodes emitting around 405 nm. In order to avoid the saturation of the spectra due to high Sm^{3+} ions doping, the measurements were performed on samples with a thickness of ~0.51 mm. Fig. 6a shows an increase in the absorption coefficient (k) as the Sm^{3+} concentration increases. Fig. 6b presents the calculated

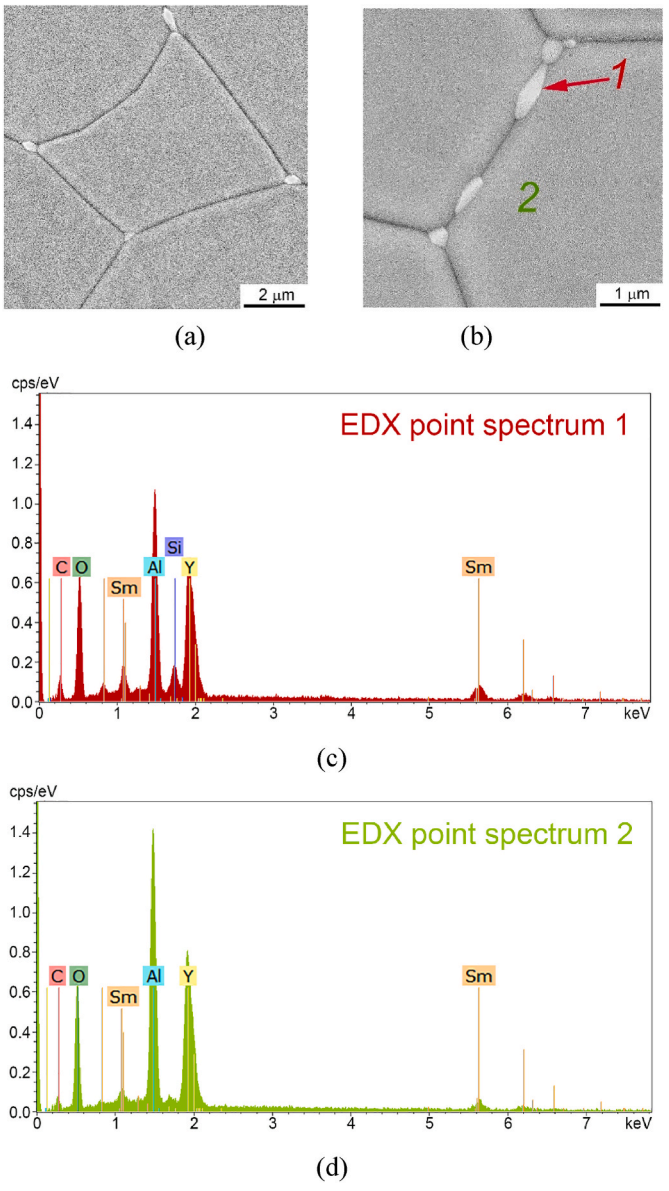

Fig. 4. FESEM images and EDX spectra of the volume and secondary phases in YAG:Sm^{3+} 11 at.% (a), and 15 at.% (b–d) ceramics sintered at 1725 °C. The numbers in Fig. 4 (b) show the location of the EDX point analysis sites: red – secondary phase composition (c), green – ceramics volume phase composition (d). (For interpretation of the references to color in this figure legend, the reader is referred to the Web version of this article.)

Table 1
Elemental composition of YAG:Sm^{3+} ceramics from 100 μm^2 area EDX analysis. The uncertainty for individual elements is caused by an EDX measurement error of about 10%. The uncertainty of the ratio calculation is determined by the maximum error given by the dispersion of the concentrations of the individual elements.

YAG: Sm^{3+}	Y (at.%)	Sm (at.%)	Al (at.%)	O (at.%)	(Y + Sm)/Al
3 at%	17.5 ± 1.8	0.6 ± 0.1	26.8 ± 2.7	55.0 ± 5.5	0.68 ± 0.16
5 at%	17.3 ± 1.7	1.0 ± 0.1	25.9 ± 2.6	55.8 ± 5.6	0.71 ± 0.19
7 at%	16.7 ± 1.7	1.3 ± 0.1	26.9 ± 2.7	55.1 ± 5.5	0.67 ± 0.15
9 at%	16.8 ± 1.7	1.8 ± 0.2	26.3 ± 2.6	55.0 ± 5.5	0.71 ± 0.16
11 at%	14.2 ± 1.4	2.0 ± 0.2	25.3 ± 2.5	58.4 ± 5.8	0.64 ± 0.14
15 at%	13.6 ± 1.4	2.9 ± 0.3	24.9 ± 2.5	59.6 ± 6.0	0.66 ± 0.15

Table 2
Elemental composition of volume and secondary phases in YAG:Sm^{3+} (15 at.%) ceramics from point EDX analysis (see Fig. 4 (b) for locations of the analysis).

YAG:Sm^{3+} (15 at.%)	Y (at. %)	Sm (at. %)	Al (at. %)	O (at. %)	Si (at. %)	Ca (at. %)	(Y + Sm)/ Al
Point 1 – secondary phase	11.6 ± 1.2	4.0 ± 0.4	20.7 ± 1.2	60.1 ± 6.0	2.7 ± 0.3	0.3 ± 0.0	0.75 ± 0.17
Point 2 – volume phase	13.5 ± 1.4	2.7 ± 0.3	24.0 ± 1.2	59.8 ± 6.0	–	–	0.68 ± 0.15

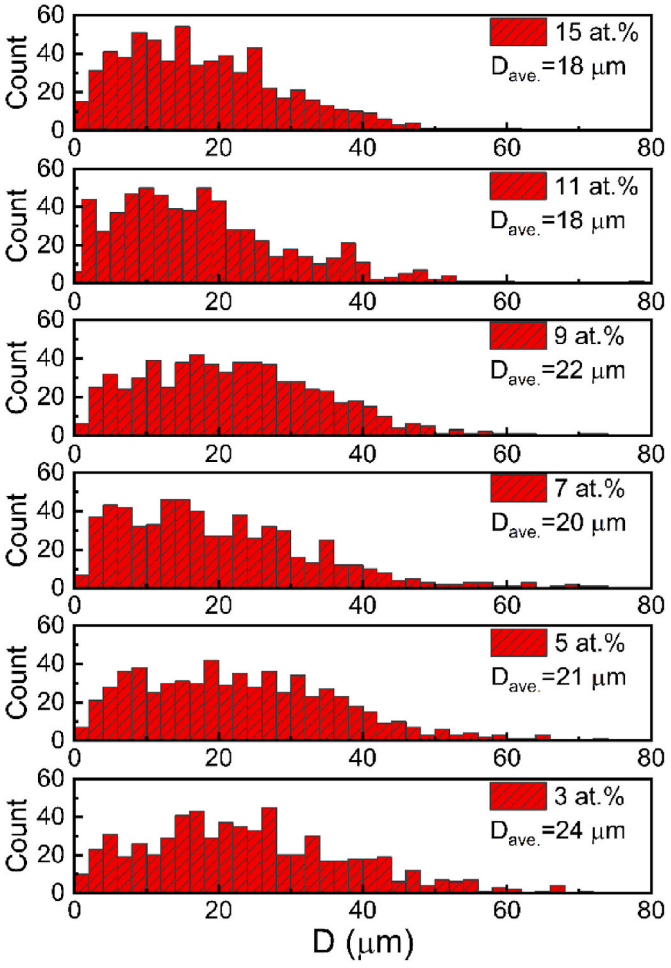

Fig. 5. Grain size distributions in YAG:Sm^{3+} transparent ceramics sintered at 1725°C and doped with different concentrations of samarium ions.

absorption cross-section (σ_{abs}) for all the samples, and the maximum value at 405.5 nm was $\sigma_{abs} = 2.8 \times 10^{20}$ cm^2 for 3 at.% Sm^{3+}. Due to the high concentration of Sm^{3+}, the absorption spectra show a small blue shift of about 0.05 nm (Fig. 6b inset) as the Sm^{3+} ions concentration increases from 3 to 15 at.%. The full widths at half maximum (FWHM) of the absorption bands around 405.5 nm increase from 0.9 to 1.05 nm corresponding to 3 and 15 at.%, respectively.

YAG:Sm^{3+} ceramics absorption spectra in the infrared (IR) region between 1000 and 1500 nm are shown in Fig. 7a. The most intense absorption lines of Sm^{3+} ions in the IR region correspond to the $^6H_{5/2} \rightarrow {}^6F_{5/2,\ 7/2,\ 9/2}$ transitions. The spectra show that as the Sm^{3+} concentration increases, the absorption coefficients and line widths increase. The blue shift of ~0.05 nm between the 3 and 15% Sm samples observed for the visible range is also present in the IR absorption spectra.

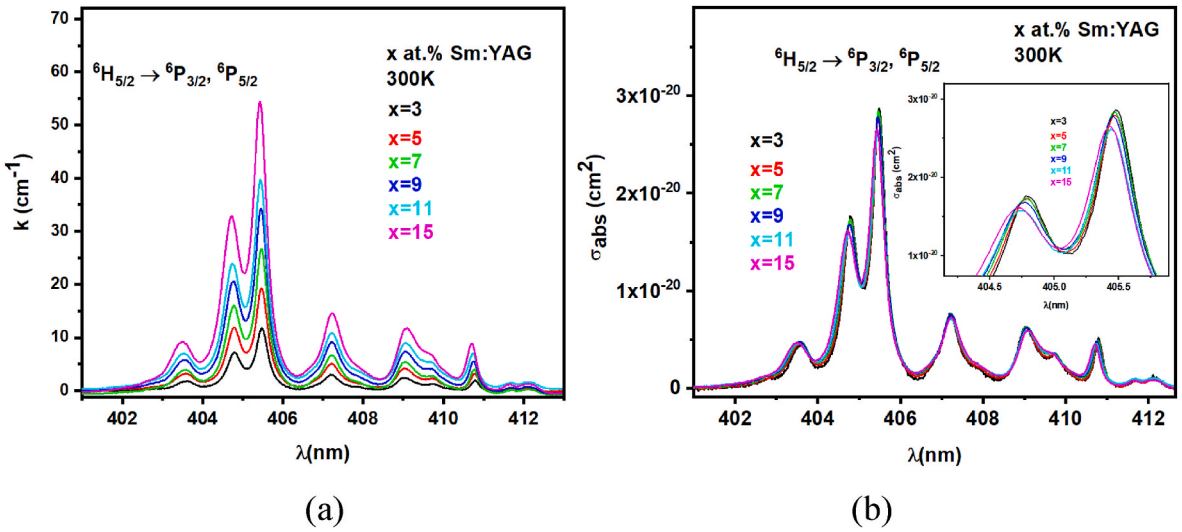

Fig. 6. The absorption spectra of Sm^{3+} in YAG:Sm^{3+} (x at.%, x = 3, 5, 7, 9, 11, and 15) ceramics (a) and the calculated absorption cross-section (σ_{abs}) (b). A small blue shift of the absorption lines is highlighted in the inset picture. (For interpretation of the references to color in this figure legend, the reader is referred to the Web version of this article.)

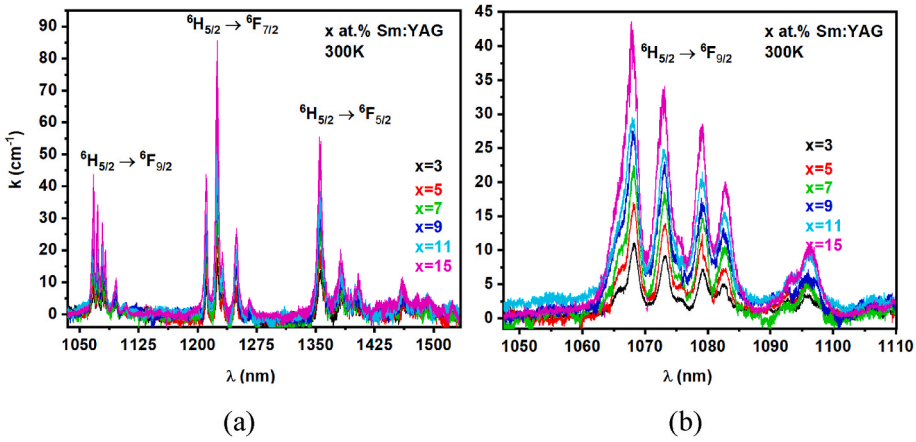

Fig. 7. The absorption spectra of Sm^{3+} in YAG:Sm^{3+} (x at.%, x = 3, 5, 7, 9, 11, and 15) ceramics in the infrared domain (a) and the absorption coefficient (*k*) corresponding to the $^6H_{5/2} \rightarrow {}^6F_{9/2}$ transition (b).

The most important transition of Sm^{3+} ions is in the range of 1050–1100 nm because the Sm^{3+} absorption in this domain overlaps with the emission of Nd^{3+} ions (~1064 nm), and is attributed to the $^6H_{5/2} \rightarrow {}^6F_{9/2}$ transition of Sm^{3+} ions. YAG:Sm^{3+} ceramics must have a sufficiently high absorption coefficient for the laser wavelength at 1064 nm to be used as an absorbing material and to suppress the parasitic oscillations due to amplified spontaneous emission (ASE) of the residual luminescence of Nd^{3+} ions.

Fig. 7b presents the evolution of the absorption coefficient (*k*) depending on Sm^{3+} ions concentration for the $^6H_{5/2} \rightarrow {}^6F_{9/2}$ transition. The spectra show that the sample with 15 at.% Sm and thickness of 0.5 mm has the highest absorption coefficients of k = 9.5 cm^{-1} at 1064 nm. This value is more than three times higher than the result of the latest study on YAG:Sm^{3+} crystal doped with 20 at.% samarium ions where the absorption coefficient was only 2.4 cm^{-1} at 1064 nm [37]. Comparing our data on 5 at.% Sm with previous results on YAG:Sm^{3+} (5 at.%) ceramics, we found an absorption coefficient of $k = 2.7$ cm^{-1} at 1064 nm, a value that is very close to the previous values reported in the literature ($k = 2.8$ cm^{-1} [32] and $k = 2.9$ cm^{-1} [34]). From Fig. 7 (b), the widening of the absorption lines can be observed due to the increase in the concentration of Sm^{3+} ions. The measured FWHM of the absorption band in the 1060–1070 nm range starts from 2 nm for the sample with 3 at.% Sm^{3+} and increases up to 2.8 nm in the case of the ceramic with 15 at.% Sm^{3+}.

As detailed in refs. [32,55], the spectral lines of RE^{3+} ions doped in YAG ($A_3B_2C_3O_{12}$) can be classified as follows: (i) main lines corresponding to the RE^{3+} ions in A position – dodecahedral sites (N lines); (ii) satellites showing dopant concentration dependence of the relative intensities and assigned to the near-neighbor (NN) and near-next neighbor (NNN) pairs of RE^{3+} ions in the A position – dodecahedral sites (M lines); (iii) satellites whose relative intensity does not depend on RE^{3+} concentration, observed only in the high-temperature crystals and assigned to the presence of the RE^{3+} ions in anomalous C position – tetrahedral sites (P lines); (iv) weak lines assigned to RE^{3+} in B position – octahedral sites (A lines). Fig. 8 shows the main absorption lines of Sm^{3+} ions in dodecahedral sites (N lines) observed for the $^6H_{5/2} \rightarrow {}^6F_{9/2}$ transition depending on the Sm^{3+} concentration at low temperature (10 K). As can be observed, for the sample doped with 3 at.% Sm^{3+} the most prominent additional lines are the M lines, and the shift from the main line is in the range of about ±(8–10) cm^{-1} depending on transition, which is in good agreement with [32]. For higher concentrations of Sm (5 and 15 at.%), the lines are broadened and the intensities of the satellite lines increase quadratically with the Sm^{3+} concentration until some of the main lines are included beneath. Also, the intensity of the

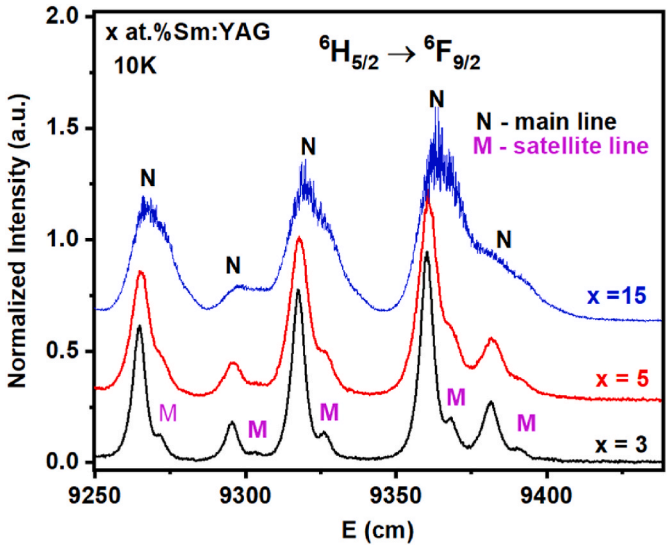

Fig. 8. Low temperature absorption spectra of YAG:Sm^{3+} ceramics (x at.%, x = 3, 5, and 15) for the $^6H_{5/2} \rightarrow {}^6F_{9/2}$ transition.

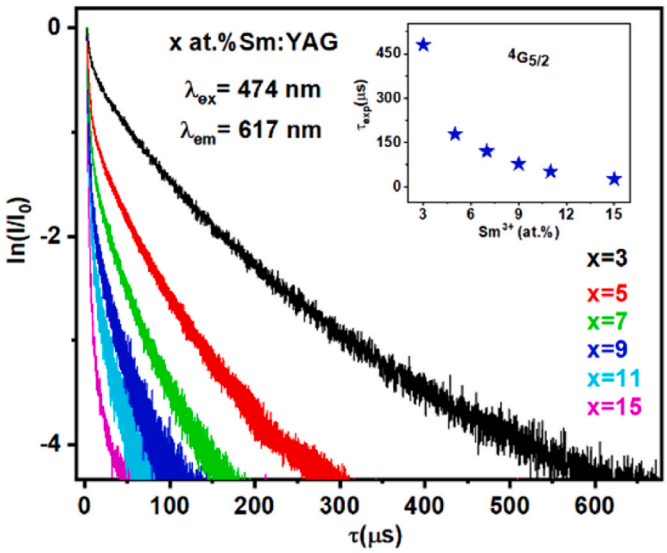

Fig. 10. Dependence of decay curves of the $^4G_{5/2}$ level of Sm^{3+} ion in YAG:Sm^{3+} (x at.%) ceramics.

absorption lines does not increase once the saturation is reached and we can observe a broadening of the lines only for 15 at.% Sm. The satellites observed near the main lines in the sample with 15 at.% Sm^{3+} contribute to the widening of the absorption lines leading to an increase in the overlap area with the emission line of Nd^{3+} at 1064 nm.

The emission spectra of Sm^{3+} ions in YAG:Sm^{3+} (x at. %) ceramic samples were obtained at 300 K under 405 nm wavelength excitation and are shown in Fig. 9a. It can be observed that the intensities of the emission lines corresponding to the $^4G_{5/2} \rightarrow {}^6H_{5/2,\ 7/2,\ 9/2,\ 11/2}$ transitions of Sm^{3+} ions decrease with increasing Sm^{3+} concentration. The high doping concentration leads to the quenching of the emission due to the increase of the energy transfer processes between Sm^{3+} ions by cross-relaxation (CR) processes of the type: CR 1 – ($^4G_{5/2} \rightarrow {}^6F_{11/2}$): ($^6H_{5/2} \rightarrow {}^6F_{5/2}$), CR 2 – ($^4G_{5/2} \rightarrow {}^6F_{9/2}$): ($^6H_{5/2} \rightarrow {}^6F_{7/2}$), CR 3 – ($^4G_{5/2} \rightarrow {}^6F_{7/2}$): ($^6H_{5/2} \rightarrow {}^6F_{9/2}$), and CR4 – ($^4G_{5/2} \rightarrow {}^6F_{5/2}$): ($^6H_{5/2} \rightarrow {}^6F_{11/2}$), as is shown in Fig. 9b [56].

The decay curves of the $^4G_{5/2}$ level of Sm^{3+} ion in YAG:Sm^{3+} (x at.%) ceramic samples were measured at 617 nm under 465 nm excitation and are shown in Fig. 10. All the decay curves are highly non-exponential due to the high Sm^{3+} ions concentration. The decays were analyzed using a double exponential equation to plot the de-excitation curves, according to the following formula:

$$I = A_1 e^{-t/\tau_1} + A_2 e^{-t/\tau_2} \tag{3}$$

where I represents the photoluminescence intensity at any time t after switching off the excitation illumination, τ_1 and τ_2 are the slow and fast decay components (long and short lifetimes), respectively, and A_1 and A_2 are the fitting (weighing factors) parameters. Using τ_1 and τ_2 values, the average lifetimes (τ_{av}) for the $^4G_{5/2}$ level were calculated with the formula:

$$\tau_{av} = \frac{A_1\tau_1^2 + A_2\tau_2^2}{A_1\tau_1 + A_2\tau_2} \tag{4}$$

The average values of the luminescence lifetimes are given in the inset of Fig. 10. The systematic dependence of the decays on Sm^{3+} concentration confirms that the quenching is due to the energy transfer between Sm^{3+} ions by cross-relaxation processes mentioned above.

The in-line optical transmittance and the calculated optical losses α_{808nm} of YAG:Sm^{3+} (3–15 at.%) transparent ceramics are shown in Fig. 11a and b, respectively. The transmittances of YAG:Sm^{3+} (3–9 at.%) specimens at 808 nm were found to be in the range of 82.5–83%, being very close to the theoretical limit of ~84.3% as determined by Fresnel reflection. For YAG:Sm^{3+} (11–15 at.%) samples, a decrease in the

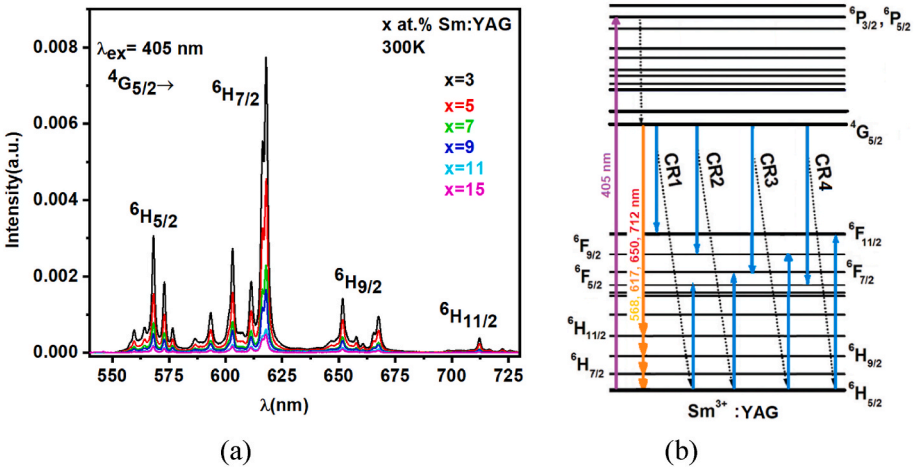

Fig. 9. Emission spectra of YAG:Sm^{3+} (x at.%) ceramics (a) and CR channels between Sm^{3+} ions (b).

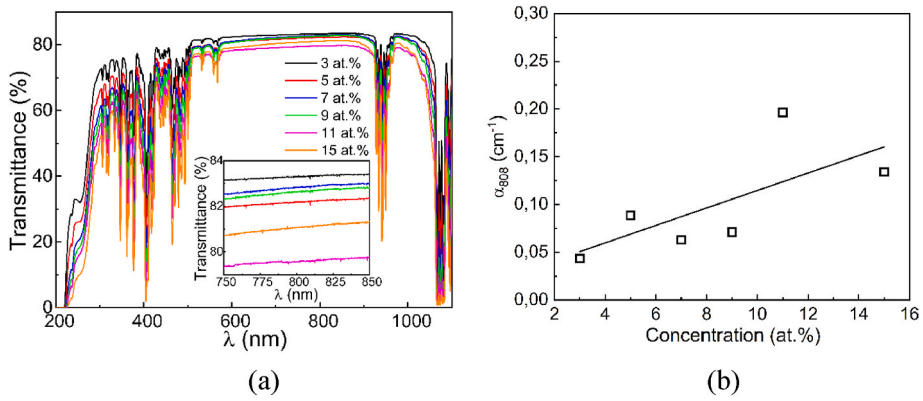

Fig. 11. In-line optical transmittance (a) and optical losses at 808 nm of YAG:Sm^{3+} (3–15 at.%) ceramics sintered at 1725 °C. The thickness of the samples is 3 mm.

transmittance to 79.5–81% was observed due to the increase in Sm^{3+} ions concentration. The degradation of optical homogeneity of the samples originates from the light scattering by residual defects (scattering centers) [57], such as pores and secondary phases detected for the 11 and 15 at.% samarium ions doping levels. The absorption coefficient of Sm^{3+} ions at 1064 nm increases with increasing Sm^{3+} concentration from 1.27 cm^{-1} for 3 at. % to 7.91 cm^{-1} in the case of 15 at.%. There are no absorption lines of Sm^{3+} ions at 808 nm, thus the optical losses at this wavelength are associated with the light scattering by residual pores and other defects. This can be used as an indicator of the optical quality of ceramics. Thus, the precipitation of the secondary phases limits the range of useful doping concentration with Sm^{3+} ions below 11 at.%. In the doping range of 3–9 at.%, the optical losses at 808 nm were found to be between 0.04 and 0.09 cm^{-1} (Fig. 11b), which is much lower than those previously reported [31]. Further increase of the Sm^{3+} ions concentration to 11 and 15 at.% leads to an increase in the optical losses at 808 nm to 0.19 cm^{-1}, mainly due to the formation of secondary phases and residual pores (Figs. 3e and f and 4a-c) [57,58].

Table 3 summarizes the optical parameters obtained on YAG:Sm^{3+} (3–15 at.%) ceramic samples. As can be observed, the highly-doped YAG:Sm^{3+} (9 at.%) ceramic (optical absorption coefficient at 1064 nm of 4.5 cm^{-1} and optical losses at 808 nm of 0.07 cm^{-1}) is a very promising material for the suppression of parasitic oscillation of YAG:Nd^{3+} lasers.

4. Conclusions

The effect of Sm^{3+} ions concentration on the structural-phase state and optical properties of reactively-sintered YAG:Sm^{3+} transparent ceramics were analyzed for the first time. The XRD investigations have shown that the YAG single-phase is formed over the entire concentration range of Sm^{3+} ions investigated. At the same time, the FESEM results revealed the precipitation of a secondary phase in YAG:Sm^{3+} ceramics doped with 11 and 15 at.% Sm^{3+}, most probably due to the decomposition of a supersaturated solid solution. Thus, the solubility limit of Sm^{3+} ions in the crystalline structure of YAG ceramics was found to be in the concentration range of 9–11 at.%. It was found that increasing the content of Sm^{3+} ions from 3 to 15 at.% leads to a decrease in the average grain size of ceramics from 24 to 18 μm due to the deformation of the crystal lattice during the introduction of larger samarium ions into the yttrium sublattice. The spectroscopic characterization of YAG:Sm^{3+} ceramic samples revealed that highly-doped samples show an increased absorption coefficient at 1064 nm. Increasing the intensity of the satellites with increasing Sm^{3+} concentration contributes to the broadening of the spectral lines and at the same time to the increase of the absorption coefficient at 1064 nm. The absorption coefficient of Sm^{3+} ions at 1064 nm increases with increasing Sm^{3+} concentration from 1.27 cm^{-1} for 3 at. % up to 7.91 cm^{-1} in the case of the doping level of 15 at.

Table 3
Optical parameters of highly-doped YAG:Sm^{3+} (3–15 at.%) transparent ceramics.

Sm^{3+} concentration (at. %)	Transmittance at 808 nm (%)	Absorption coefficient at 1064 nm (cm^{-1})	Optical losses at 808 nm (cm^{-1})
3	83.3	1.27	0.04
5	82.2	2.29	0.09
7	82.9	3.28	0.06
9	82.7	4.45	0.07
11	79.6	5.42	0.19
15	81.1	7.91	0.13

%. The optical losses at 808 nm in the Sm^{3+} doping range of 3–9 at.% were found to be between 0.04 and 0.09 cm^{-1}, while for higher Sm^{3+} concentration (11 and 15 at.%) the optical losses increase up to 0.19 cm^{-1} due to the formation of secondary phases and residual pores. The obtained results demonstrate that highly-doped YAG:Sm^{3+} (9 at.%) transparent ceramic having an optical absorption coefficient at 1064 nm of 4.45 cm^{-1} and optical losses at 808 nm of 0.07 cm^{-1} could be the best candidate for parasitic oscillation suppression in high-power YAG:Nd^{3+} lasers at 1064 nm.

Declaration of competing interest

The authors declare that they have no known competing financial interests or personal relationships that could have appeared to influence the work reported in this paper.

Acknowledgments

This work was supported by the National Academy of Sciences of Ukraine within the departmental academic Project “Masshtab-2” (2022-2024). The CERIC-ERIC consortium is acknowledged for financial support under Project number 20202040. The authors are grateful to D.A. Cherkashin for help in characterizing the ceramic samples.

References

[1] A. Ikesue, T. Kinoshita, K. Kamata, K. Yoshida, Fabrication and optical properties of high-performance polycrystalline Nd:YAG ceramics for solid-state lasers, J. Am. Ceram. Soc. 78 (1995) 1033–1040, https://doi.org/10.1111/j.1151-2916.1995.tb08433.x.
[2] R.M. Springer, M.E. Thomas, Analysis and comparison of single crystal and polycrystalline Nd:YAG, absorption, IEEE J. Quant. Electron. 49 (2013) 667–676, https://doi.org/10.1109/JQE.2013.2269026.
[3] R.M. Springer, M.E. Thomas, R.I. Joseph, Analysis and comparison of single-crystal and polycrystalline Nd:YAG, scatter, IEEE J. Quant. Electron. 51 (8) (2015), https://doi.org/10.1109/JQE.2015.2442761, 1700408–1700408.
[4] H. Yagi, T. Yanagitani, T. Numazawa, K. Ueda, The physical properties of transparent $Y_3Al_5O_{12}$: elastic modulus at high temperature and thermal

conductivity at low temperature, Ceram. Int. 33 (2007) 711–714, https://doi.org/10.1016/j.ceramint.2005.12.007.
[5] R. Yasuhara, H. Furuse, A. Iwamoto, J. Kawanaka, T. Yanagitani, Evaluation of thermo-optic characteristics of cryogenically cooled Yb:YAG ceramics, Opt. Express 20 (2012) 29531–29539, https://doi.org/10.1364/OE.20.029531.
[6] J. Hostaša, J. Matějíček, B. Nait-Ali, D.S. Smith, W. Pabst, L. Esposito, Thermal properties of transparent Yb-doped YAG ceramics at elevated temperatures, J. Am. Ceram. Soc. 97 (8) (2014) 2602–2606, https://doi.org/10.1111/jace.13015.
[7] H. Furuse, R. Yasuhara, K. Hiraga, Thermal properties of transparent Yb-doped YAG ceramics at elevated temperatures, Thermo-optic properties of ceramic YAG at high temperatures, Opt. Mater. Express 4 (2014) 1794–1799, https://doi.org/10.1364/OME.4.001794.
[8] A.A. Kaminskii, Laser crystals and ceramics: recent advances, Laser Photon. Rev. 1 (2) (2007) 93–177, https://doi.org/10.1002/lpor.200710008.
[9] V. Lupei, A. Lupei, A. Ikesue, Transparent polycrystalline ceramic laser materials, Opt. Mater. 30 (11) (2008) 1781–1786, https://doi.org/10.1016/j.optmat.2008.03.003.
[10] A. Ikesue, Y. Aung, Ceramic laser materials, Nat. Photonics 2 (2008) 721–727, https://doi.org/10.1038/nphoton.2008.243.
[11] J. Sanghera, W. Kim, G. Villalobos, B. Shaw, C. Baker, J. Frantz, B. Sadowski, I. Aggarwal, Ceramic laser materials, Materials 5 (2) (2012) 258–277, https://doi.org/10.3390/ma5020258.
[12] J. Li, Y.B. Pan, Y.P. Zeng, W.B. Liu, B.X. Jiang, J.K. Guo, The history, development, and future prospects for laser ceramics: a review, Int. J. Refract. Metals Hard Mater. 39 (2013) 44–52, https://doi.org/10.1016/2Fj.ijrmhm.2012.10.010.
[13] K. Takaichi, H. Yagi, J. Lu, A. Shirakawa, K. Ueda, T. Yanagitani, A.A. Kaminskii, Yb^{3+}-doped $Y_3Al_5O_{12}$ ceramics – a new solid-state laser material, Phys. Status Solidi 200 (2003), https://doi.org/10.1002/pssa.200309016. R5–R7.
[14] J. Dong, A. Shirakawa, K. Ueda, H. Yagi, T. Yanagitani, A.A. Kaminskii, Efficient Yb^{3+}:$Y_3Al_5O_{12}$ ceramic microchip lasers, Appl. Phys. Lett. 89 (2006), 091114, https://doi.org/10.1063/1.2345229.
[15] G. Boulon, Why so deep research on Yb^{3+}-doped optical inorganic materials? J. Alloys Compd. 451 (2008) 1–11, https://doi.org/10.1016/j.jallcom.2007.04.148.
[16] J. Dong, K. Ueda, H. Yagi, A.A. Kaminskii, Z. Cai, Comparative study the effect of Yb concentrations on laser characteristics of Yb:YAG ceramics and crystals, Laser Phys. Lett. 6 (2009) 282–289, https://doi.org/10.1002/lapl.200810136.
[17] F. Tang, Y. Cao, W. Guo, Y. Chen, J. Huang, Z. Deng, Z. Liu, Z. Huang, Fabrication and laser behavior of the Yb:YAG ceramic microchips, Opt. Mater. 33 (2011) 1278–1282, https://doi.org/10.1016/j.optmat.2011.02.049.
[18] J. Dong, G. Xu, J. Ma, M. Cao, Y. Cheng, K. Ueda, H. Yagi, A.A. Kaminskii, Investigation of continuous-wave and Q-switched microchip laser characteristics of Yb:YAG ceramics and crystals, Opt. Mater. 34 (2012) 959–964, https://doi.org/10.1016/j.optmat.2011.05.005.
[19] A.J. Stevenson, E.R. Kupp, G.L. Messing, Low temperature, transient liquid phase sintering of B_2O_3-SiO_2-doped Nd:YAG transparent ceramics, J. Mater. Res. 26 (9) (2011) 1151–1158, https://doi.org/10.1557/jmr.2011.45.
[20] J. Lu, K. Ueda, H. Yagi, T. Yanagitani, Y. Akiyama, A.A. Kaminskii, Neodymium doped yttrium aluminum garnet ($Y_3Al_5O_{12}$) nanocrystalline ceramics – a new generation of solid state laser and optical materials, J. Alloys Compd. 341 (2002) 220–225, https://doi.org/10.1016/S0925-8388(02)00083-X.
[21] J. Liu, Q. Liu, J. Li, X. Ba, W. Liu, H. Kou, B. Jiang, Y. Pan, X. Cheng, High doping Nd:YAG transparent ceramics fabricated by solid-state reactive sintering, Phys. Status Solidi 10 (2013) 933–939, https://doi.org/10.1002/pssc.201300001.
[22] W. Jing, S. Yu, X. Ji, T. Xu, B. Kang, J. Deng, W. Yin, Z. Yao, H. Huang, Preparation of a Φ60 mm Nd:YAG transparent ceramic disk, Ceram. Int. 43 (6) (2017) 5334–5337, https://doi.org/10.1016/j.ceramint.2016.11.170.
[23] R. Boulesteix, C. Chevarin, R. Belon, A. Maître, L. Cochain, C. Sallé, Manufacturing of large size and highly transparent Nd:YAG ceramics by pressure slip-casting and post-sintering by HIP: an experimental and simulation study, Materials 13 (9) (2020) 2199, https://doi.org/10.3390/ma13092199.
[24] S. Zamir, The influence of cation additives on grain-boundary mobility in yttrium aluminum garnet (YAG), J. Am. Ceram. Soc. 98 (1) (2015) 324–330, https://doi.org/10.1111/jace.13290.
[25] R. Boulesteix, A. Maitre, L. Chretien, Y. Rabinovitch, C. Sallé, Microstructural evolution during vacuum sintering of yttrium aluminum garnet transparent ceramics: toward the origin of residual porosity affecting the transparency, J. Am. Ceram. Soc. 96 (2013) 1724–1731, https://doi.org/10.1111/jace.12315.
[26] A.J. Stevenson, X. Li, M.A. Martinez, J.M. Anderson, D.L. Suchy, E.R. Kupp, E. C. Dickey, K. Mueller, G.L. Messing, Effect of SiO_2 on densification and microstructure development in Nd:YAG transparent ceramic, J. Am. Ceram. Soc. 94 (5) (2010) 1380–1387, https://doi.org/10.1111/j.1551-2916.2010.04260.x.
[27] W. Kong, M. Tsunekane, T. Taira, Diode edge-pumped passively Q-switched microchip laser, Opt. Eng. 54 (9) (2015), 090501, https://doi.org/10.1117/1.OE.54.9.090501.
[28] Y.F. Ma, Y. He, X.D. Li, X. Yu, L. Ge, J. Li, R.P. Yan, R. Sun, Continuous-wave and passively Q-switched tape casting YAG/Nd:YAG/YAG ceramic laser, Opt. Mater. Express 6 (9) (2016) 2966–2974, https://doi.org/10.1364/OME.6.002966.
[29] Z. Zhu, S. Lv, H. Zhang, Y. Hui, H. Lei, Q. Li, Highly efficient actively Q-switched Nd:YAG laser, Opt Express 29 (20) (2021) 32326–32332, https://doi.org/10.1364/OE.438414.
[30] F. Tian, A. Ikesue, J. Li, Progress and perspectives on composite laser ceramics: A review, J. Eur. Ceram. Soc. 42 (5) (2022) 1833–1851, https://doi.org/10.1016/j.jeurceramsoc.2021.12.061.
[31] H. Yagi, J.F. Bisson, K. Ueda, T. Yanagitani, $Y_3Al_5O_{12}$ ceramic absorbers for the suppression of parasitic oscillation in high-power Nd:YAG lasers, J. Lumin. 121 (2006) 88–94, https://doi.org/10.1016/j.jlumin.2005.10.006.
[32] A. Lupei, V. Lupei, C. Gheorghe, A. Ikesue, Spectroscopic investigation of Sm^{3+} in YAG ceramic, Rom, Rep. Phys. 63 (2011) 817–822.
[33] A. Lupei, V. Lupei, C. Gheorghe, Thermal shifts of Sm^{3+} lines in YAG and cubic sesquioxide ceramics, Opt. Mater. Express 3 (2013) 1641–1646, https://doi.org/10.1364/OME.3.001641.
[34] K. Hamamoto, S. Tokita, H. Yoshida, N. Miyanaga, J. Kawanaka, Temperature-dependent absorption assessment of YAG ceramics as cladding material, Opt. Mater. Express 8 (2018) 2378–2386, https://doi.org/10.1364/OME.8.002378.
[35] H. Ali, T.H. Maram, A. Kana, M.A. Khedr, Spectroscopy and optical properties of Sm^{3+}:YAG nanocrystalline powder prepared by co-precipitation method: effect of Sm^{3+} ions concentrations, Open J. Appl. Sci. 4 (2014) 96–102, https://doi.org/10.4236/ojapps.2014.43011.
[36] R. Skaudzius, S. Sakirzanovas, A. Kareiva, On the samarium substitution effects in $Y_{3-x}Sm_xAl_5O_{12}$ (x=0.1–3.0), J. Electron. Mat. 47 (7) (2018) 3951–3956, https://doi.org/10.1007/s11664-018-6277-7.
[37] M. Němec, J. Šulc, H. Jelínková, A. Zavadilová, K. Nejezchleb, N. Kapitch, Samarium-doping concentration influence on spectroscopic parameters of Sm:YAG crystal, Proc. SPIE 11259 (2020), 1125921, https://doi.org/10.1117/12.2544604.
[38] A.D. Timoshenko, A.G. Doroshenko, S.V. Parkhomenko, I.O. Vorona, O. S. Kryzhanovska, N.A. Safronova, O.O. Vovk, A.V. Tolmachev, V.N. Baumer, I. Matolínova, R.P. Yavetskiy, Effect of the sintering temperature on microstructure and optical properties of reactive sintered YAG:Sm^{3+} ceramics, Opt. Mater. X 13 (2022), 100131, https://doi.org/10.1016/j.omx.2021.100131.
[39] M. Inoue, H. Otsu, H. Kominami, T. Inui, Glycothermal synthesis of rare earth aluminium garnets, J. Alloys Compd. 226 (1995) 146–151, https://doi.org/10.1016/0925-8388(95)01632-5.
[40] B. Strocka, P. Holst, W. Tolksdorf, An empirical formula for the calculation of lattice constants of oxide garnets based on substituted yttrium-and gadolinium-iron garnets, Philips J. Res. 33 (1978) 186–202.
[41] M.S. Nikova, V.A. Tarala, F.F. Malyavin, I.S. Chikulina, D.S. Vakalov, A. A. Kravtsov, S.O. Krandievsky, V.A. Lapin, E.V. Medyanik, L.V. Kozhitov, S. V. Kuznetsov, Sintering and microstructure evolution of $Er_{1.5}Y_{1.5-x}Sc_{x+y}Al_{5-y}O_{12}$ garnet ceramics with scandium in dodecahedral and octahedral sites, J. Eur. Ceram. Soc. 42 (5) (2022) 2464–2477, https://doi.org/10.1016/j.jeurceramsoc.2022.01.008.
[42] Database of ionic radii [Electronic resource], http://abulafia.mt.ic.ac.uk/shannon/ptable.php.
[43] R.D. Shannon, C.T. Prewitt, Effective ionic radii and crystal chemistry, J. Inorg. Nucl. Chem. 32 (5) (1970) 1427–1441, https://doi.org/10.1016/0022-1902(70)80629-7.
[44] A. Ikesue, K. Kamata, Role of Si on Nd solid-solution of YAG ceramics, J. Ceram. Soc. Jpn. 103 (5) (1995) 489–493, https://doi.org/10.2109/jcersj.103.489.
[45] M.N. Rahaman, Sintering of Ceramics, CRC Press, 2007, p. 392, https://doi.org/10.1201/b15869.
[46] A. Ikesue, Y.L. Aung, T. Taira, T. Kamimura, K. Yoshida, G.L. Messing, Progress in ceramic lasers, Annu. Rev. Mater. Res. 17 (36) (2006) 397–429, https://doi.org/10.1146/annurev.matsci.36.011205.152926.
[47] M. Tachibana, A. Iwanade, K. Miyakawa, Distribution coefficient of rare-earth dopants in $Y_3Al_5O_{12}$ garnet, J. Cryst. Growth (2021) 568–569, https://doi.org/10.1016/j.jcrysgro.2021.126191, 126191.
[48] D.C. Brown, K. Kowalewski, V. Envid, J. Zembek, J.W. Kolis, C.D. McMillen, H. Geisber, Advanced smart multifunctional laser crystals for next generation solid state lasers, Proc. SPIE 8381 (2012), 838108, https://doi.org/10.1117/12.921434.
[49] A. Ikesue, K. Kamata, K. Yoshida, Effects of neodymium concentration on optical characteristics of polycrystalline Nd:YAG laser materials, J. Am. Ceram. Soc. 79 (1996) 1921–1926, https://doi.org/10.1111/j.1151-2916.1996.tb08014.x.
[50] D. Yu Kosyanov, R.P. Yavetskiy, V.N. Baumer, Yu L. Kopylov, V.B. Kravchenko, I. O. Vorona, A.I. Cherednichenko, V.I. Vovna, A.V. Tolmachev, Effect of Nd^{3+} ions on phase transformations and microstructure of 0–4 at.% Nd^{3+}:$Y_3Al_5O_{12}$ transparent ceramics, J. Alloys Compd. 686 (2016) 526–532, https://doi.org/10.1016/j.jallcom.2016.06.046.
[51] J. Poledniа, R. Dohmen, K. Marquardt, Grain boundary diffusion and its relation to segregation of multiple elements in yttrium aluminum garnet, Eur. J. Mineral 32 (2020) 675–696, https://doi.org/10.5194/ejm-32-675-2020.
[52] V.I. Chani, G. Boulon, W. Zhao, T. Yanagida, A. Yoshikawa, Correlation between segregation of rare earth dopants in melt crystal growth and ceramic processing for optical applications, Jpn. J. Appl. Phys. 49 (2010), 075601, https://doi.org/10.1143/JJAP.49.075601.
[53] A. Ikesue, Y.L. Aung, V. Lupei, Ceramic lasers, Cambridge University Press, 2013, https://doi.org/10.1017/CBO9780511978043.
[54] S. Singh, I. Gupta, D. Singh, Sm^{3+}-activated YAG nanocrystals: synthesis, structural and spectroscopic analysis for orange-red emitting LEDs, Optik 238 (2021), 166482, https://doi.org/10.1016/j.ijleo.2021.166482.
[55] V. Lupei, A. Lupei, C. Tiseanu, S. Georgescu, C. Stoicescu, P.M. Nanau, High-resolution optical spectroscopy of YAG:Nd: A test for structural and distribution models, Phys. Rev. B 51 (1) (1995) 8–17, https://doi.org/10.1103/PhysRevB.51.8.

[56] I. Gupta, S. Singh, S. Bhagwan, D. Singh, Rare earth (RE) doped phosphors and their emerging applications: A review, Ceram. Int. 47 (2021) 19282–19303, https://doi.org/10.1016/j.ceramint.2021.03.308.
[57] S. Hribalova, W. Pabst, Modeling light scattering by spherical pores for calculating the transmittance of transparent ceramics – All you need to know, J. Eur. Ceram. Soc. 41 (2021) 2169–2192, https://doi.org/10.1016/j.jeurceramsoc.2020.11.046.
[58] R. Boulesteix, A. Maître, J.F. Baumard, Y. Rabinovitch, F. Reynaud, Light scattering by pores in transparent Nd:YAG ceramics for lasers: Correlations between microstructure and optical properties, Opt. Express 18 (2010) 14992–15002, https://doi.org/10.1364/OE.18.014992.